frontiers in Physics

ORIGINAL RESEARCH
published: 21 September 2021
doi: 10.3389/fphy.2021.750097

Spectral Evolution of an Eruptive Polar Crown Prominence With IRIS Observations

Jianchao Xue [1], *Hui Li* [1,2]* *and Yang Su* [1,2]

[1]Key Laboratory of Dark Matter and Space Astronomy, Purple Mountain Observatory, Chinese Academy of Sciences, Nanjing, China, [2]School of Astronomy and Space Science, University of Science and Technology of China, Hefei, China

Prominence eruption is closely related to coronal mass ejections and is an important topic in solar physics. Spectroscopic observation is an effective way to explore the plasma properties, but the spectral observations of eruptive prominences are rare. In this paper we will introduce an eruptive polar crown prominence with spectral observations from the Interface Region Imaging Spectrograph (IRIS), and try to explain some phenomena that are rarely reported in previous works. The eruptive prominence experiences a slow-rise and fast-rise phase, while the line-of-sight motions of the prominence plasma could be divided into three periods: 2 hours before the fast-rise phase, opposite Doppler shifts are found at the two sides of the prominence axis; then, red shifts dominate the prominence gradually; in the fast-rise phase, the prominence gets to be blue-shifted. During the second period, a faint component appears in Mg II k window with a narrow line width and a large red shift. A faint region is also found in AIA 304 Å images along the prominence spine, and the faint region gets darker during the expansion of the spine. We propose that the opposite Doppler shifts in the first period is a feature of the polar crown prominence that we studied. The red shifts in the second period are possibly due to mass drainage during the elevation of the prominence spine, which could accelerate the eruption in return. The blue shifts in the third period are due to that the prominence erupts toward the observer. We suggest that the faint component appears due to the decreasing of the plasma density, and the latter results from the expansion of the prominence spine.

Keywords: Sun: corona, Sun: coronal mass ejections (CMEs), Sun: filaments, prominences, Sun: UV radiation, techniques: spectroscopic

OPEN ACCESS

Edited by:
HengQiang Feng,
Luoyang Normal University, China

Reviewed by:
Leping Li,
National Astronomical Observatories (CAS), China
Pavol Schwartz,
Astronomical Institute of Slovak Academy of Sciences, Slovakia

***Correspondence:**
Hui Li
nj.lihui@pmo.ac.cn

Specialty section:
This article was submitted to Stellar and Solar Physics, a section of the journal Frontiers in Physics

Received: *30 July 2021*
Accepted: *06 September 2021*
Published: *21 September 2021*

Citation:
Xue J, Li H and Su Y (2021) Spectral Evolution of an Eruptive Polar Crown Prominence With IRIS Observations. Front. Phys. 9:750097. doi: 10.3389/fphy.2021.750097

1 INTRODUCTION

Solar prominences are composed of cold and dense plasma suspended in the hot corona [1–4]. Prominence eruptions have a close relationship with flares and coronal mass ejections (CMEs), and the latter two phenomena are main causes of the space weather storms. Hence studying the triggering mechanism and evolution of prominence eruptions are important topics in solar physics. Spectroscopic observation is an effective way to reveal plasma properties and line-of-sight (LOS) motions. However, high-quality spectral data of eruptive prominences are rare due to limited field of view (FOV) of general spectroscopic observations and randomness of prominence eruptions.

The Interface Region Imaging Spectrograph (IRIS [5]), is a small explorer spacecraft launched in 2013 June. It provides simultaneous high-resolution spectral and imaging data from the photosphere to the corona. The IRIS especially has an advantage of observing chromosphere and transition region

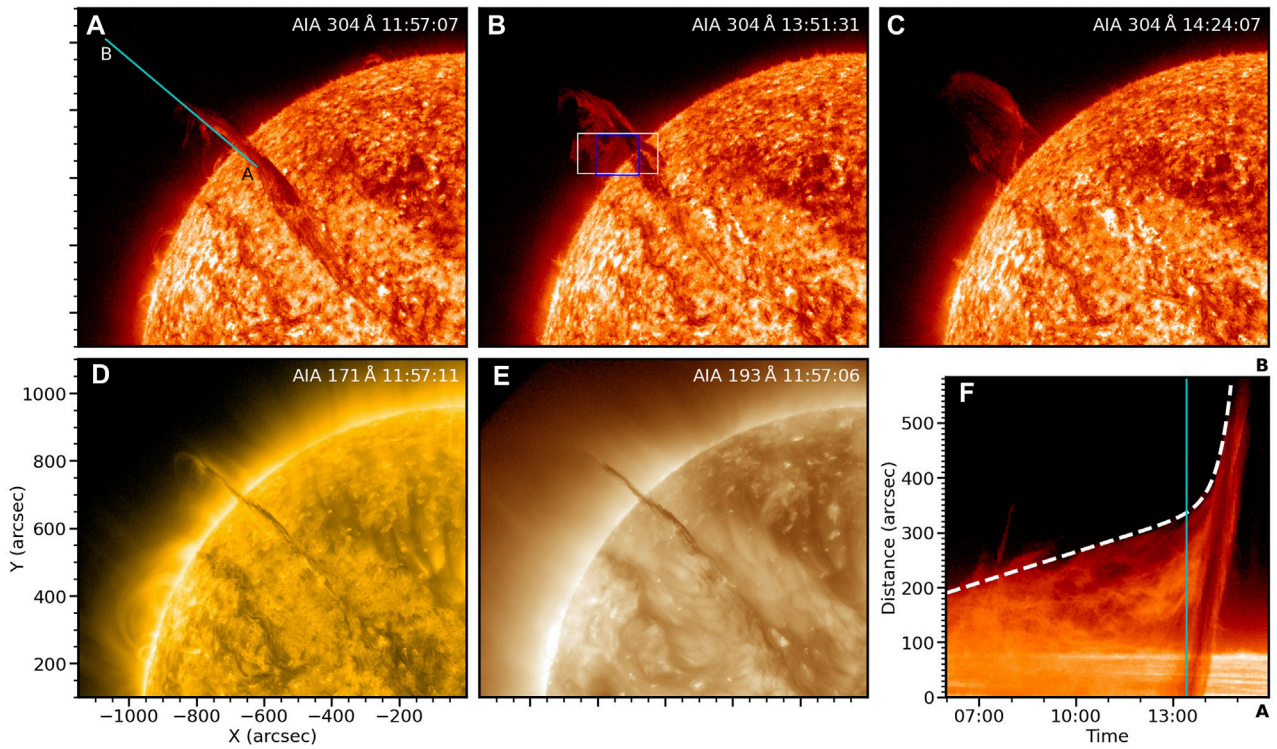

FIGURE 1 | Evolution of the eruptive prominence in EUV images. **(A–C)** AIA 304 Å images. The cyan slice AB in **(A)** is the position of the time-distance diagram in panel **(F)**. The white box in **(B)** represents the FOV of IRIS SJI observations, and the blue box marks the FOV of spectroscopic observations. **(D–E)** AIA 171 and 193 Å images, respectively. **(F)** Time-distance diagram along the slice AB in panel **(A)** from AIA 304 Å images. The cyan line marks the onset of the fast-rise phase.

with some strong resonance lines of Mg II (temperature of formation of log T [K] ~ 4.0), C II (log T [K] ~ 4.3), and Si IV (log T [K] ~ 4.8). The prominence core has a chromospheric temperature, and prominence also has a prominence-corona transition region (PCTR). So the IRIS is also suitable to observe prominences and filaments. The IRIS has been widely used to study the dynamics of quiescent prominences [6–9], but the spectroscopic observations of eruptive prominences are still rare. Among the few works [10], reported an erupting prominence in active region using IRIS observations; the authors found a faint component with **a** LOS velocity up to 460 km s^{-1}, and revealed the unwinding motions during the prominence eruption [11]. studied an eruptive prominence in quiet region with radiative transfer computations; they derived the electron densities of the prominence between 1.3×10^9 and 6.0×10^{10} cm^{-3}, the mean temperature around 1.1×10^4 K, and the total hydrogen mass between 1.3×10^{14} and 3.2×10^{14} g.

In this work, we focus on the spectral evolution of an eruptive polar crown prominence (the prominence located at high latitude) on 2015 April 28th, which erupts successfully with a CME. The high-quality IRIS observations reveal some phenomena that have not been reported, and we try to give reasonable explanations on them. This event was studied by Reference [12] using extreme ultraviolet (EUV) images, who were interested in the outflows within the dimming region and proposed that the outflows are the origin of CME-induced solar wind. Dai et al. (submitted) used EUV images to explore the eruption mechanism of this event, and thought that the eruption is related to the prominence oscillation and mass drainage. Our paper is organized as follows: **Section 2** introduces the observations and data reduction; **Section 3** shows the prominence eruption process and **its** spectral features; we give our explanations on some observed phenomena in **Section 4**, which is followed by conclusion in **Section 5**.

2 OBSERVATIONS AND DATA REDUCTION

An eruption of a polar crown prominence on 2015 April 28th was well observed by the IRIS. **Figure 1A-E** show the snapshots of the eruptive prominence in EUV images from the Atmospheric Imaging Assembly (AIA [13]), onboard the Solar Dynamics Observatory (SDO [14]). The observational channels and times are denoted in each panel. The IRIS observations were carried out between 10:59–14:54 UT with 24 large coarse raster scans, and each scan had 64 × 2″ raster steps. The binned pixel size along the raster slit is 0.33″, the same as the slit width. The resulting FOV is 126″ × 119″ centered at – 742″ east and 666″ north (see the blue rectangle in **Figure 1B**). In the snapshot of **a** slit-jaw image (SJI) **at** 2796 Å in **Figure 2A**, the dashed white lines mark the slit position No.30 (left), upper boundary of the FOV of the Mg II raster

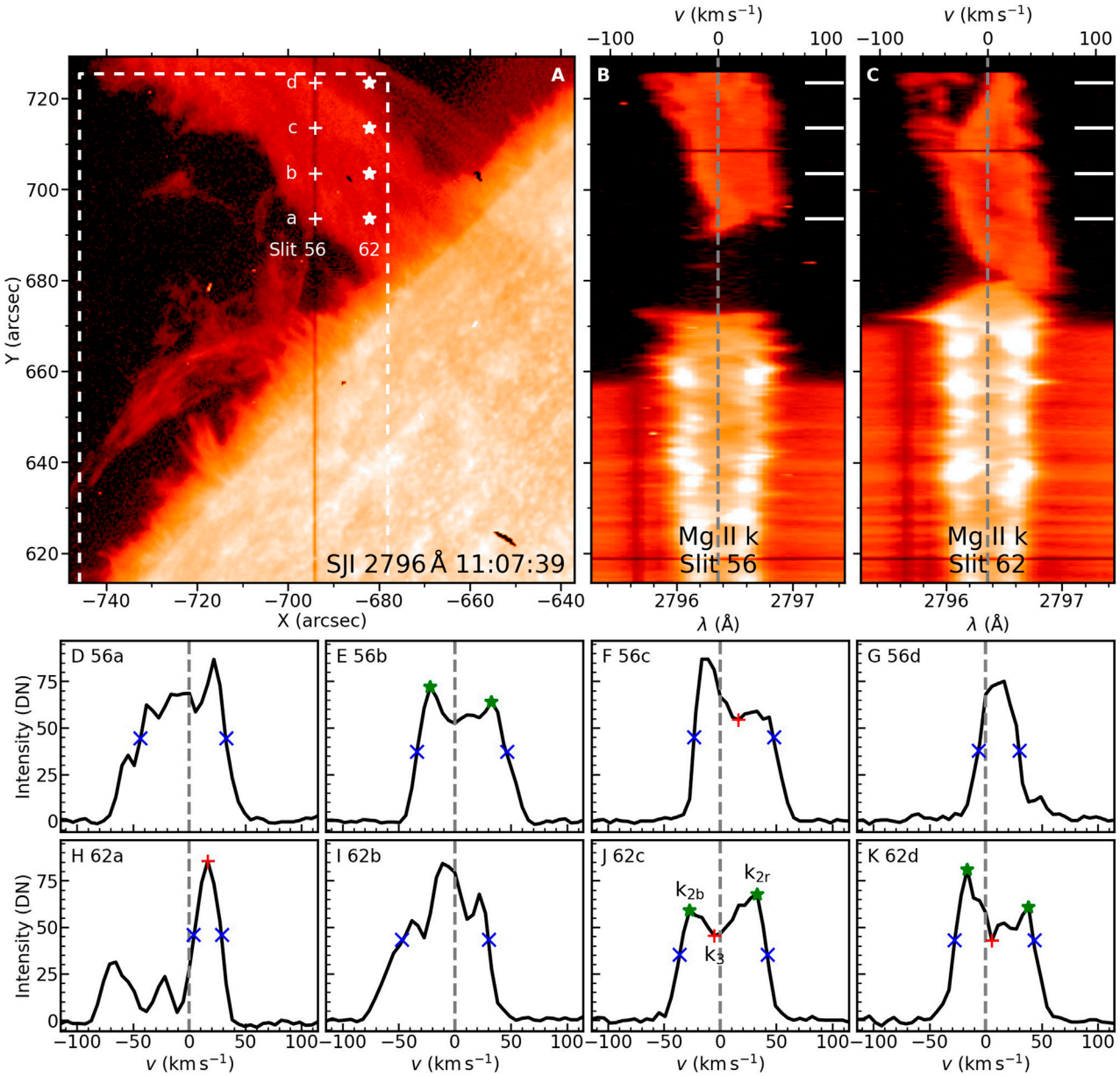

FIGURE 2 | Estimation of LOS velocities from Mg II k line profiles. **(A)** SJI 2796 Å. The dashed white lines mark the slit position No.30 **(left)**, upper boundary of the FOV of Mg II raster **(top)**, and the slit position No.64 **(right)**. Eight points marked by plus or star symbols are chosen for analysis in panels **(D–K)**. **(B–C)** Images of the Mg II k spectra along the **slit** positions No.56 (at 11:07:39 UT) and 62 (at 11:08:44 UT), respectively. The short white lines mark the positions of the spectra in panels **(D–K)**. The vertical dashed lines represent the rest wavelength of the Mg II k line. **(D–K)** Mg II k profiles at the positions marked in panels **(A–C)**. The red pluses represent the positions of k_3, the green stars represent k_2, and the blue × symbols represent the positions of half maximum.

(top), and the slit position No.64 (right). The exposure time of each raster is 8 s and the step cadence is 9.2 s. The spectral resolution is ~ 5.5 km s^{-1} with binned pixels. The slit occurs at the center of SJIs in Solar-X direction. The FOV of each SJI is 117″ × 119″, and FOV of SJI observations is marked in **Figure 1B** with the white rectangle. The SJIs at 2796, 1400, and 1330 Å are available, which have a cadence of ~ 37 s and the binned pixel size is 0.333 arcsec in each channel. We mainly use SJIs 2796 Å and 1400 Å, the former has a passband of 4 Å centered at 2796 Å, mainly contributed by the Mg II k line; the latter has a passband of 55 Å centered at 1390 Å, mainly contributed by Si IV lines but also including O IV lines, etc.

IRIS level 2 data are used, for which dark current and offsets are removed, flat field is corrected, and geometric and wavelength calibrations (for spectrograph channels) are done. The FOV of SJIs is checked by comparing them with the AIA 304 Å images. The spatial position of spectra is shifted along Solar-Y slightly "using the fiducial marks on the slit" as suggested by the referee.

(see **Figure 2B** at 618″ and 708″, respectively). The wavelength calibrations are checked using lines Ni I 2799.474 Å in the Mg II window and Fe II 1392.82 Å in the Si IV window radiated from the solar disk; the wavelength errors are expected to be within 2 km s^{-1}. For images of the Si IV 1394 Å line spectra, bright and isolated pixels are identified as spikes, and their values are replaced by their surrounding mean values. Errors of spectral intensities from signal uncertainty and readout noise are considered. The former is set to be square root of photon number, and the conversion coefficient from digital number (DN) to photons is 18 for near ultraviolet (NUV, including the Mg II k line), and 4 for far ultraviolet (FUV, including the Si IV 1394 Å line). The readout noise is related to dark current uncertainty, which is set to be 1.8 DN for NUV (from the negative values in data) and 3.3 DN for FUV [5].

EUV images from the SDO/AIA and LOS magnetograms from the SDO/HMI (Helioseismic and Magnetic Imager [15]), are used. The former has pixel size of 0.6″ and temporal resolution of 12 s; the latter has pixel size of 0.5″. Both AIA and HMI images are processed to level 1.5.

2.1 Estimation of Prominence LOS Velocity

It is almost impossible to describe LOS (Doppler) velocities of a prominence strictly, due to that a prominence consists of many threads with different velocities [6, 8]. For optically thin lines, such as Si IV 1394 Å, double Gaussian fitting could give two averaged LOS velocities. For optically thick lines, such as Mg II k/h and H I Lyman series, the profiles are often centrally reversed due to self-absorption, and effects of non-LTE (departure from the local thermodynamic equilibrium) should be considered [16–19]. Despite these difficulties, we could still obtain some information of LOS velocities from the optically thick lines Reference [20]. proposed that for reversed profiles of Mg II k/h lines, the Doppler shift of the central minimum (or the maximum for a purely emission profile, called k_3 for the k line, see **Figure 2J**) correlates strongly with the LOS velocity at the $\tau = 1$ height of the line core (τ represents the optical thickness), and the average Doppler shift of the peaks (called k_{2b} and k_{2r} for the blue and red sides of the peaks, respectively) correlates with the LOS velocity at the average $\tau = 1$ height of the peaks (deeper than the formation height of the line core). LOS velocity also affects the asymmetry of the peaks [18]. However, it is often difficult to identify the positions of k_{2b}, k_{2r}, and k_3 for complex profiles.

The center of gravity (COG) method can be used to derive the Doppler shifts of purely absorption (photospheric lines [21]) or purely emission lines. When there are multi-velocity components in a spectral profile, the COG method gives a weighted average result. However, the COG method is physically wrong for the emission profiles with central reversals, although this method is sometimes still useful in such case [11]. The COG method is expressed as

$$v_D = \frac{\sum_i (I(v_i) - C)v_i}{\sum_i (I(v_i) - C)}, \quad (1)$$

TABLE 1 | Estimation of LOS velocities of the eight profiles shown in **Figure 2D–K** using different methods: shift of k_3, average shift of k_{2b} and k_{2r}, average shift at half maximum, and COG. The velocities are in the unit of "km s^{-1}".

Method	56a	56b	56c	56d	62a	62b	62c	62d
k_3	-	-	16	-	16	-	–5	6
k_3	-	6	-	-	-	-	3	11
Half maximum	–6	6	12	11	16	–9	3	8
COG	–7.1	6.9	11.3	13.4	–11.6	–10.8	3.6	6.1

NOTE–The given accuracies of the calculated velocities using the shift of k_3, average shift of k_2, and average shift at half maximum are 1 km s^{-1} due to that the spectral resolution is ≈5.5 km s^{-1}, and the accuracies using the COG method are 0.1 km s^{-1} because around 40 pixels are considered.

where v_D is Doppler velocity, I is intensity, C is continuum, and wavelength λ is converted into velocity (v) in the unit of "km s^{-1}" using

$$v_i = \frac{\lambda_i - \lambda_0}{\lambda_0} c, \quad (2)$$

in which λ_0 is the rest wavelength and c is the light speed.

To check the reliability of the COG method, we compare it with the methods proposed by Ref. [20]. **Figure 2A** is a slit-jaw 2796 Å image during the first scan, and **Figures 2B,C** show the images of the Mg II k line spectra along slit positions No.56 (at 11:07:39 UT) and No.62 (at 11:08:44 UT), respectively. Four points along the slit position No.56 and four along the No.62 are chosen (denoted with "a", "b", "c", "d" for different heights in panel (A)), and their Mg II k line profiles are plotted in **Figures 2D-K** sequentially. Positions of k_3 (marked with the red plus symbols) and k_2 (marked with the green stars) are identified when there is no much confusion. We also calculate the average shift at half maximum for each profile (marked with the blue × symbols). The results are listed in **Table 1**. From the images of the spectra in **Figure 2B-C**, it is intuitive that the top part along the slit position No.56 is slightly blue-shifted and the lower part of the prominence is red-shifted; along the slit position No.62, the top part has multi-velocity components and the lower part is also red-shifted. Among the eight line profiles in **Figure 2D-K**, the positions of k_3 are only identified in four profiles, and three of them are even questionable (56c, 62c, and 62d). So the LOS velocities derived from k_3 are also questionable. The positions of k_{2b} and k_{2r} are determined in three profiles relatively precisely. The average shift at half maximum is calculated for each profile, and the results are consistent with what we see in the image of the spectra. However, this method may not include weak components as in case of the profiles from Positions 56a and 62a (**Figures 2D,H**). The LOS velocities derived from the COG method have the same signs as those derived from the average shifts of peaks or at half maximum except the 62a profile due to the aforementioned reason. The results of the COG method are also consistent with the images of the spectra, which means that this method is not influenced by occurrence of central reversals for the chosen profiles.

We will see that some Mg II k line profiles are reversed deeply during the prominence eruption. In most cases, the signs of LOS

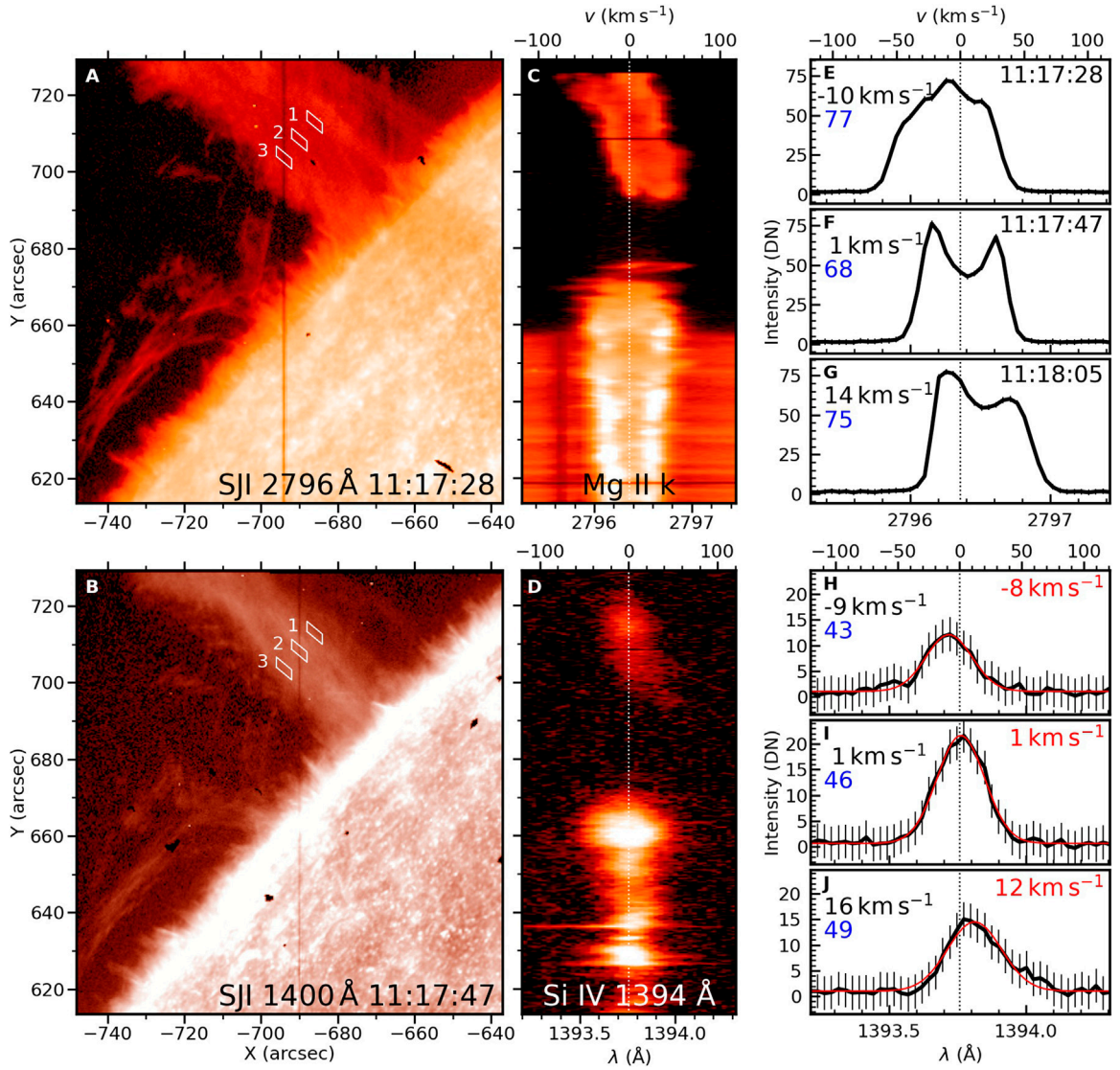

FIGURE 3 | Spectral observations around 11:17 UT. First column: IRIS SJIs. Second column: images of the spectra at the slit position as shown in panel **(A)**. Third column: average spectral profiles from boxes 1-3tbox1-3 in panels **(A–B)**, sequentially. The first row is for **Mg II** observations and the second row is for the Si iv window. The vertical dotted lines in **(C–J)** mark the positions of rest wavelengths. In panels **(E–J)**, Doppler velocities derived from the COG method (black fonts) and FWHMs in the units of "km s^{-1}" (blue fonts) are noted in left. In panels **(H–J)**, the Doppler velocities derived from Gaussian fitting (red curves) are marked in right (red fonts).

velocities derived from the COG method are generally consistent with the images of the spectra. We will give quantitative results using Gaussian fitting or directly from the images of the spectra, and use the COG method to derive LOS velocities statistically (not physically for profiles with self-absorption) and qualitatively.

3 RESULTS

3.1 Eruption Overview

The long filament, when the prominence is seen against the solar disk, extends from nearly solar disk center to beyond the northeastern solar limb on 2015 April 28th. **Figure 1A–E** show its EUV images, including the eruption process in AIA 304 Å. When seen in AIA 171 and 193 Å (**Figure 1D–E**), the prominence is thinner than that seen in AIA 304 Å (**Figure 1A**) due to lower opacities. A part of the prominence is blocked by itself before the prominence eruption (**Figure 1A**), and LOS is mainly along the prominence axis for IRIS observations. In **Figure 1B**, the prominence is erupting; a dark region along the filament spine and two bright ribbons on the solar disk can be seen. In **Figure 1C**, the prominence erupts further, and its spine inclines toward the solar equator. We synthesize a time-distance diagram in AIA 304 Å along the slice AB in **Figure 1A**, and the result is shown in **Figure 1F**. We fit the prominence height in **Figure 1F** with a slow-rise phase (linear function) and a fast-rise phase (exponential function) using the approximation [22, 23].

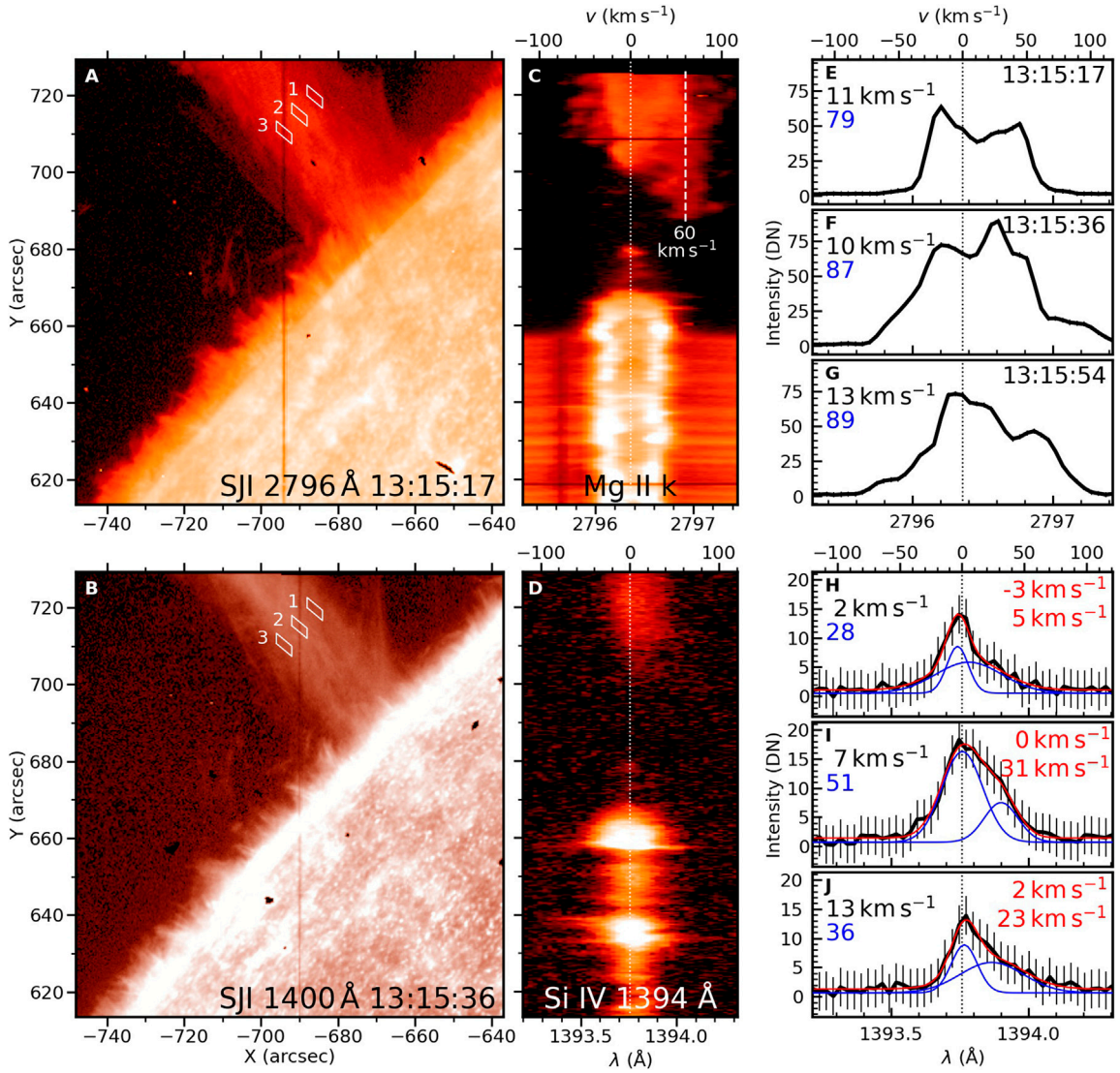

FIGURE 4 | Spectral observations around 13:15 UT. The layout is similar to **Figure 3** but double Gaussian fitting is used for Si IV 1394 Å line profiles in panels **(H–J)**, where blue curves show separate Gaussian components.

$$h(t) = c_0 e^{(t-t_0)/\tau} + c_1 (t - t_0) + c_2, \tag{3}$$

where h represents height, t is time, t_0 is arbitrary, and τ, c_0, c_1, c_2 are parameters obtained by fitting. The obtained initial rise speed is $c_1 = 3.78\ \mathrm{km\ s^{-1}}$, and the erupting speed at the end of our tracking is ~ 103 km s^{-1}. Onset of the fast-rise phase is defined by

$$t_{\mathrm{onset}} = \tau \ln\left(\frac{c_1 \tau}{c_0}\right) + t_0, \tag{4}$$

which is calculated to be 13:25:30 UT (the cyan vertical line in **Figure 1F**).

3.2 Spectral Evolution

We have seen in **Figure 2** around 11:07 UT that the top part of the raster is slightly blue-shifted and the lower part of the prominence is red-shifted. In this section, we will introduce the spectral evolution, especially the variations of LOS velocities of the erupting prominence in detail. **Figure 3** shows IRIS observations around 11:17 UT (the second raster scan), including SJI snapshots (**Figure 3** left column), images of the spectra along the dark slit in **Figure 3A** (middle), and spectral profiles (right) of the Mg II k line (upper part) and the Si IV line (lower part), respectively. Comparing the prominence images in the two wavelengths, SJI 1400 Å has a narrower bright core with faint prominence edges (**Figure 3B**) than SJI 2796 Å (**Figure 3A**), and the Si IV 1394 Å line profiles (**Figure 3H–J**) are weaker with lower signal-to-noise ratios (S/N) than the Mg II k line (**Figure 3E–G**). Mg II k line **profiles** are sometimes reversed (**Figure 3F–G**), while Si IV 1394 Å line profiles can be fitted using a Gaussian profile (red curves in **Figure 3H–J**). Besides, the Mg II k line has a larger line width than the Si IV 1394 Å, despite that the latter is formed at a higher temperature. These performances are

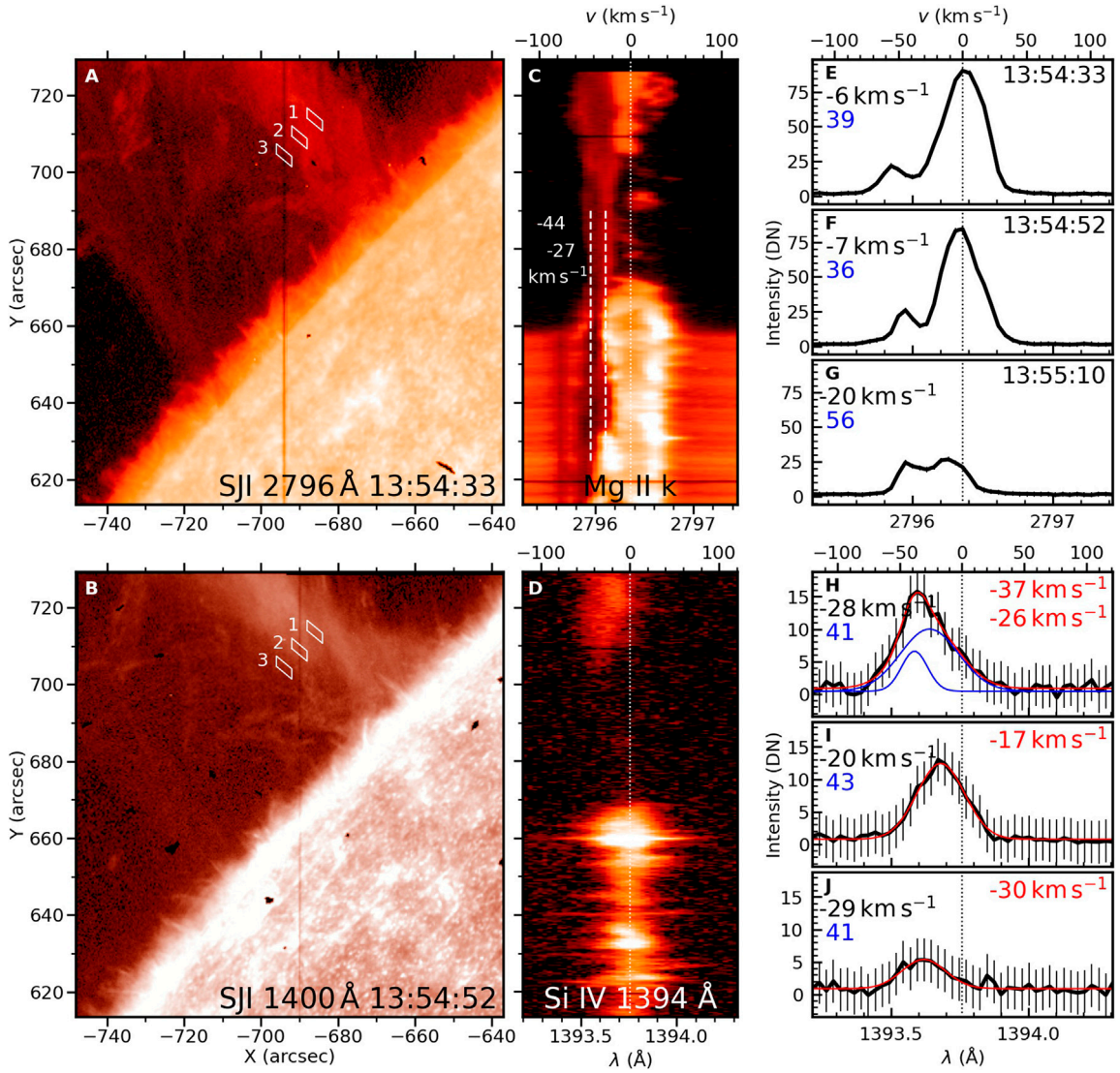

FIGURE 5 | Spectral observations around 13:54 UT, similar to **Figures 3**, **4**.

mainly due to that the Mg II k line has a larger opacity than the Si IV 1394 Å.

In both of the images of the Mg II k and Si IV 1394 Å spectra in **Figure 3C, D**, the blue-shifted top part and red-shifted lower part are visible. We choose three regions in **Figure 3A, B** from right to left with respect to the prominence axis, and their average spectral profiles are plotted in **Figure 3E–J**. In these panels, the Doppler velocities derived from the COG method (black fonts) and the full widths at half maximum (FWHMs, blue fonts, in the unit of "km s^{-1}") are denoted at the left. In **Figure 3H–J** for the Si IV 1394 Å line profiles, the Doppler velocities from Gaussian fitting are denoted at the right (red fonts). Both Mg II k and Si IV 1394 Å lines show that the right part of the prominence is blue-shifted, with the Doppler velocity of −8.4 ± 0.7 km s^{-1} (**Figure 3H** using single Gaussian fitting); the left part is red-shifted, with the Doppler velocity of 11.7 ± 0.8 km s^{-1} (**Figure 3J**).

The prominence spectra vary obviously when the prominence approaches eruption. The layout of **Figure 4** is similar to **Figure 3** but observed at ~13:15 UT, about 10 min before the onset of the fast-rise phase. In **Figures 4C,** a red-shifted (around 60 km s^{-1}) faint component appears, which can be seen in SJI at the prominence edges (**Figure 4A, B**). The Mg II k line profiles in **Figure 4E–G** are red-asymmetry with multi-velocity components, and another red Gaussian profile is necessary to fit the Si IV 1394 Å line profiles in **Figure 4H–J**. With more velocity components, the line widths get wider, and FWHM of the Mg II k line is nearly 90 km s^{-1} (**Figure 4F, G**), and that of the Si IV 1394 Å line is around 50 km s^{-1} (**Figure 4I**). However, the Mg II k line of the faint component has a narrower width around 30 km s^{-1} (**Figure 4C**).

During the fast-rise phase in **Figure 5**, the faint components changes to be blue-shifted, with two main Doppler velocities

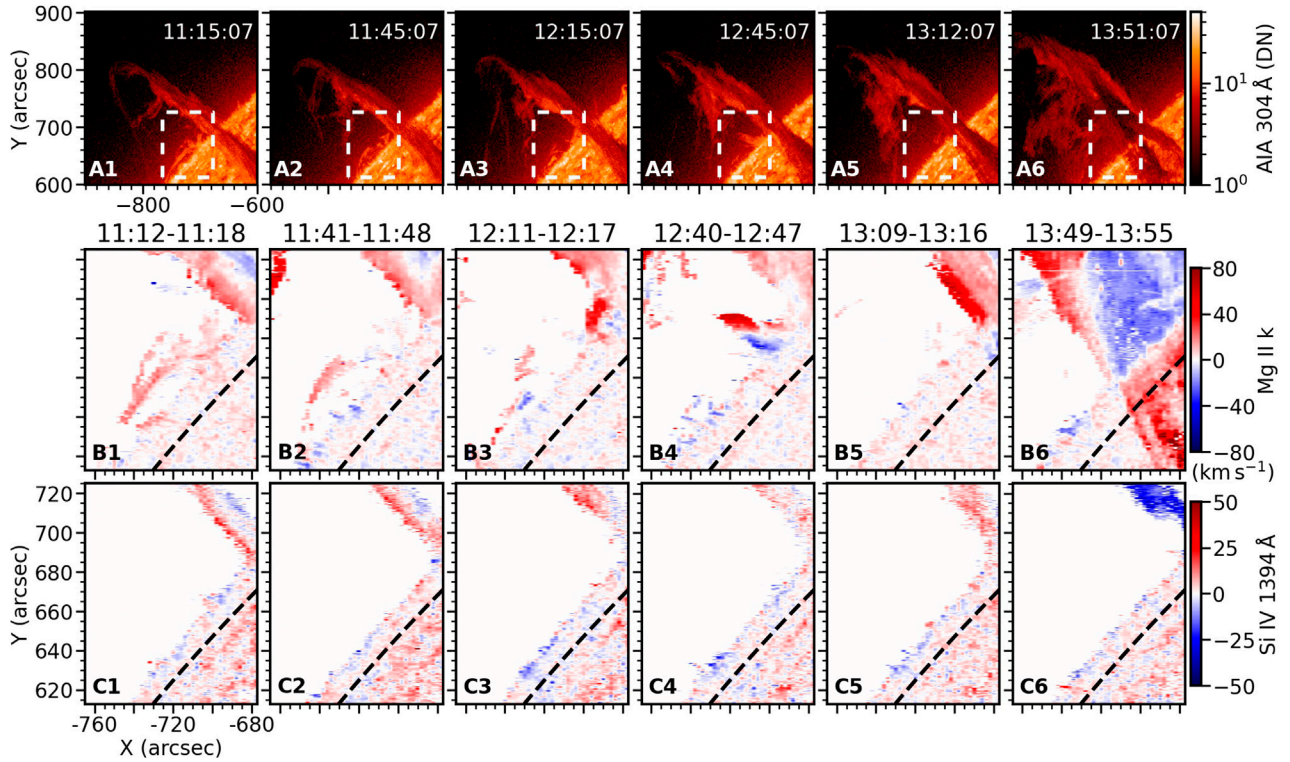

FIGURE 6 | Doppler images derived from the spectra of Mg II k (first row) and Si IV 1394 Å (second row) using the COG method. First row: the AIA 304 Å images. Second and third rows: Doppler images from the Mg II k and the Si IV 1394 Å lines, respectively. Each Doppler image is composed of 44 raster steps from the slit position No.21 **(left)** to the slit position No.64 **(right)**, and the observation times of the two slits are denoted above. The dashed black lines represent the solar limb. Color bars are shown at the right for each row.

shown in the image of the Mg II k line spectra (**Figure 5C**): -44 and −27 km s^{-1}. In the image of Si IV 1394 Å spectra in **Figure 5D**, the bright component is also obviously blue-shifted, and the Gaussian fitting results show that the Doppler velocity is at least −17 km s^{-1} (**Figure 5I**). However, the bright component in Mg II k has no obvious shift (**Figure 5C**), and the line widths are small (**Figure 5E, F**). We will see in next section that it is due to the absorption by the faint component. The emission of the box 3 in the SJI 2796 Å (**Figure 5A**) is mainly from the faint component, which is identified from the weak emission of the Mg II k line with blue shifts (**Figure 5G**). The weak emission of the Si IV 1394 Å line from the box 3 (**Figure 5J**) with the similar blue shift suggests that the Si IV line has a contribution to the brightness of the faint component in SJI 1400 Å.

To analyze the evolution of the prominence LOS velocities in detail, we calculate Doppler images from both the Mg II k and Si IV 1394 Å lines using the COG method. After the calculations, isolated noises in the Doppler images are further removed.

The obtained Doppler images are shown in **Figure 6**, where the first row shows AIA 304 Å images and the dashed boxes mark the FOV of the Doppler images in the lower two rows. Initially (the first column in **Figure 6**), the left part of the prominence is red-shifted and the right part is mainly blue-shifted with a boundary near the prominence axis; the maximum red-shifted velocity is ~ 30 km s^{-1}, and the maximum blue-shifted velocity is ~ 20 km s^{-1} from both Mg II k and Si IV 1394 Å Doppler images (the difference is < 2 km s^{-1}). Then, red shifts dominate the prominence gradually, and the largest Doppler shifts always occur at the left edge. At around 13:15 (**Figure 6**B5), there is a largely red-shifted region corresponding with the faint component as shown in **Figure 4A, B**. About 25 min after the onset of the fast-rise phase (the rightmost column in **Figure 6**), the erupting prominence is mainly blue-shifted, and the average and maximum LOS velocities in Si IV 1394 Å window are 22 and 47 km s^{-1}, respectively. The blue-shifted velocities in Mg II k window are smaller, and red shifts can still be seen at the left edge. Note that in the Mg II k Doppler image in **Figure 6**B6, the positive values along the filament on the solar disk result from the fact that part of the blue wing of the Mg II k line, which is radiated from the solar disc, is absorbed by the erupting filament (see **Figure 5C**).

3.3 Faint Component

A detailed view on the evolution of the faint component is shown in **Figure 7**, where the AIA 304 Å images at different times are shown in the first row, the slit-jaw 2796 Å images are shown in the second row, the third row shows images of the Mg II k line spectra along the slit positions in **Figure 7B**, and the remaining two rows show Mg II k profiles at the positions marked in **Figure 7C**. Panels C-E share the same abscissa but in different units. At 12:55:39 UT (the first column in **Figure 7**), the regions

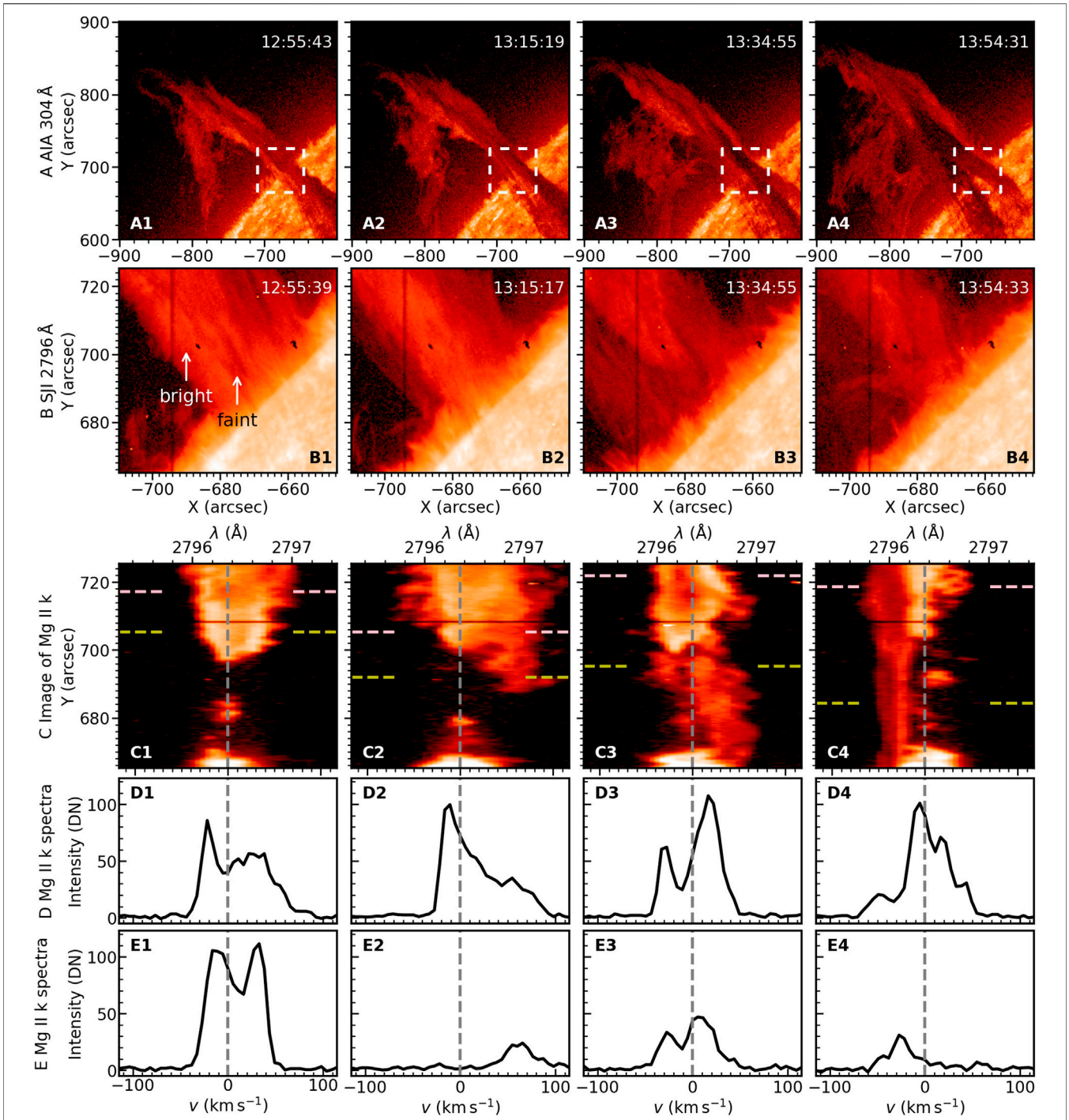

FIGURE 7 | AIA 304 Å and Mg II k observations focusing on faint components. **(A)** The AIA 304 Å images. The dashed boxes represent the FOV of the snapshots in panels **(B)**. **(B)** The slit-jaw 2796 Å images. **(C)** Images of the Mg II k spectra at the slit positions as shown in images in panels **(B)**. **(D)** Mg II k profiles from the positions marked with dashed pink lines in panels **(C)**. **(E)** Mg II k profiles from the positions marked with dashed yellow lines in panels **(C)**.

with or without the faint components can be differed in both AIA 304 Å and SJI 2796 Å. In **Figure 7**C1, the lower part of prominence spectrum is not blended by the faint component, which is reversed with two clear peaks (**Figure 7**(e1)); but the upper part is overlaid with the faint component and the peak at the red wing is absorbed with some weak peaks (**Figure 7**(d1)). Twenty min later (the second column in **Figure 7**, the same time as **Figure 4**), the faint component is significantly red-shifted. From **Figure 7**C2, we can see that the largest Doppler velocity of red-shifted component is beyond 100 km s^{-1}. The Mg II k line in

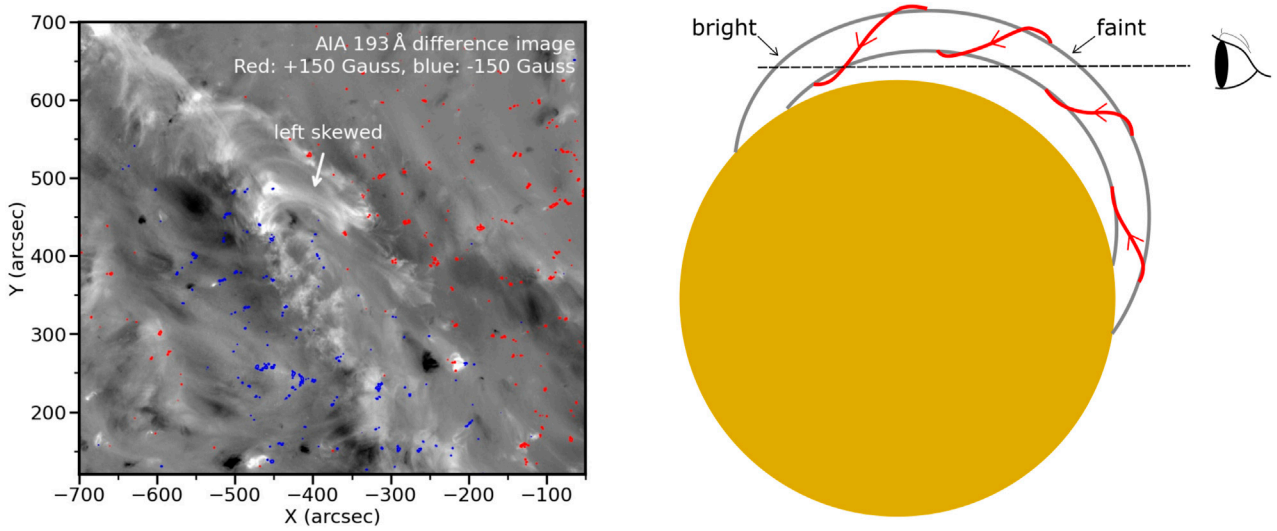

FIGURE 8 | Prominence chirality and view. **(A)** AIA 193 Å difference image by the image observed at 16:00:06 UT subtracting the one at 11:57:06 UT. The red and blue contours mark LOS magnetic field ±150 Gauss, respectively, from HMI observed at 15:59:05 UT. **(B)** Cartoon showing the prominence viewing angle. The red arrows represent the magnetic helicity with exaggerated twist number.

Figure 7D2 includes information of both bright and faint components; it also peaks at blue wing and the red wing is absorbed. At 13:34:55 UT, about 10 min after the onset of fast-rise phase (the third column in **Figure 7**), the sign of Doppler shifts of the faint component is changing: the lower part is mainly red-shifted but the upper part is blue-shifted (**Figure 7**C3). The Mg II k line in **Figure 7**D3 is seriously reversed, and the ratio of line peak to central minimum is 4.5. As a comparison, the ratio of the profile in **Figure 7**E1 is 1.7. At 13:54:33 UT (the fourth column in **Figure 7**, the same time as **Figure 5**), the faint component is blue-shifted, and the blue wing of the bright component is absorbed. When focusing on the AIA 304 Å images, we can see the darkening of the faint region during the eruption process. The expansion of the faint prominence spine is visible in both AIA 304 Å and SJI 2796 Å.

4 DISCUSSION

The prominence eruption in the FOV of SDO/AIA can be divided into slow- and fast-rise phases, and the onset of the fast-rise phase is around 13:25 UT. However, The prominence Doppler shifts experience three periods: 1) 2 hours before the fast-rise phase, the left part of prominence, with respect to the prominence axis, is red-shifted and the right part is mainly blue-shifted (first column in **Figure 6**); 2) then, red-shifted area increases, and almost the whole prominence (in IRIS FOV) is red-shifted at 10 min before the fast-rise phase; 3) during the fast-rise phase, the prominence gets to be blue-shifted. A faint component is clearly identified at 12:55:39 UT (first column in **Figure 7**). The faint component in Mg II k window has a narrow line width (~ 30 km s^{-1}, **Figure 4**) and significant variations of Doppler shifts. Besides, the faint component can absorb the radiation from the bright part, which leaves a single profile peak when the faint component has a significant Doppler shift, or results in a deep central reversal when the shift is slight. In Si IV window, the faint component can still be identified in SJI despite the lower S/N; two Gaussian profiles are necessary to fit the Si IV 1394 Å line profiles when the bright component is overlapped with the faint component in LOS. The faint region along the prominence spine in AIA 304 Å images is spatially related to the faint component. The darkening and expansion of the faint region during the prominence eruption are visible. The faint component is also red-shifted before the fast-rise phase, with a larger LOS velocity than the bright component. In the fast-rise phase, the faint component gets to be blue-shifted, too. In the following sections, we will give our explanations on these phenomena.

4.1 Magnetic Configuration and View of the Prominence

A knowledge about the magnetic configuration and viewing angle of the prominence is helpful for understanding its observational features. The left image in **Figure 8** is a AIA 193 Å difference image overlaid with LOS magnetogram contours of ±150 Gauss. The post-eruption loops is left skewed, which suggests that the filament channel has a negative magnetic helicity [24]. Hence, we plot the cartoon of the filament as a flux rope [25] with an exaggerated twist number for a clear view (the right image in **Figure 8**). Due to the fact that the faint component can absorb Mg II k radiation from the bright component, the faint component should be in front, which could also be seen in AIA 304 Å images (**Figure 7A**).

4.2 Causes of Doppler Evolutions

Opposite Doppler shifts observed in a same prominence are generally explained as counter-streaming. In previous observations of counter-streaming, bidirectional flows were seen thread by thread [26], or blue- and red-wing images showed different directional flows [27]. Some of counter-streaming observations could be explained by local motions of plasma, such as small-scale oscillations [28] or magnetic reconnection [29]. In our event, the opposite Doppler shifts are found from the beginning of IRIS observations, and are possibly a property of the polar crown prominence that we studied. A major difference from previous observations is that the opposite Doppler shifts are distributed much regularly, i.e., the left half is red-shifted and the right part is mainly blue-shifted. This phenomenon reveals large-scale flows along the prominence spine, and cannot be explained by the local plasma motions.

Unidirectional flows along the flux rope could also cause opposite Doppler shifts when the LOS is perpendicular to the flux rope axis [24, 30–32]. Despite that the LOS is mainly along the prominence spine in the FOV of the IRIS in our case, we assume that the opposite Doppler shifts are caused by the flows within the spine. In this case, in the cartoon of **Figure 8**, the flows of the part marked with "bright" should move toward the observer, or the flows marked with "faint" should move away from the observer, or both, to cause the left being red-shifted and the right being blue-shifted with respect to the prominence axis. In the following period, the spine is dominantly red-shifted, but the blue shifts are not enhanced. The different evolutions of the red and blue shifts makes this assumption questionable.

During the fast-rise phase in the third column in **Figure 7**, the faint component shows opposite Doppler shift along the slit, which is possibly caused by untwisting motion of the erupting prominence [10], which could be seen in AIA 304 Å images by tracking the faint region (**Figure 7**).

When approaching the fast-rise phase, red shifts dominate the prominence, and the faint component has a large LOS velocity. In the Mg II k window, the LOS velocity of the bright component is not clear due to the fact that its emission is absorbed partly by the faint component. But from the Si IV window, the results of the double Gaussian fitting (**Figure 4H–J**) suggest that the Doppler shift of the bright component is not obvious. The red shifts could be explained by the mass drainage during the elevation of the prominence spine, which could accelerate the prominence eruption in return [33]. In our case, if the prominence mass moves toward the prominence footpoint behind the solar disk, the direction of LOS velocity is consistent with the red shifts (see the cartoon in **Figure 8**). The large Doppler velocity of the faint component suggests that the mass near the spine center moves faster than the mass near the footpoint, which is possibly due to more significant elevation of the prominence spine center, and that the large density near the footpoint may slow down the flows.

During the fast-rise phase, the prominence gets to be blue-shifted, which reveals the overall movement of the erupting prominence away from the solar disk and toward the observer.

4.3 Formation of the Faint Component

Reference [10] did also observe a faint and narrow component with a large Doppler velocity up to 460 km s^{-1} in an erupting active region prominence. The authors proposed that the two components with different Doppler velocities suggest that the erupting material is distributed in a hollow cone shape. The faint component in our observations share most of features as reported by Reference [10]; despite that the Doppler velocity is relatively small. In addition, there are some phenomena only seen in our observations. Firstly, we could see the faint component in AIA 304 Å images and SJIs directly, hence we observed darkening and expansion of the faint component during the prominence eruption (**Figure 7A, B**). Besides, we observed that the faint component can absorb the Mg II k radiation from the bright component. On the basis of these phenomena, we suspect that the Mg II k line from the faint component has a lower opacity than that from the bright component, and the faint component is composed of low-density and cold plasma due to the expansion of the prominence spine.

The intensity ratio of Mg II k and h lines is widely used to check the opacity [7, 10, 11, 20]: the ratio is generally in the range of 1–2, and approaches 2 under the optically thin assumption and gets small with the increase of opacity. **Figure 9** shows the images of Mg II k integrated intensity (panels A,B) and k/h ratio (panels C,D) from spectral observations. Continuum intensity is subtracted when calculating the images. The left column in **Figure 9** is observed between 11:13 UT and 13:19 UT before the occurrence of the faint component, and the k/h ratio is relatively homogeneous. A region is selected in **Figure 9C** with yellow box, and the mean k/h ratio is 1.25. The right column in **Figure 9** is observed between 13:11 UT and 13:17 UT, and a faint region is seen at the prominence left edge (**Figure 9B**). The k/h ratio image in **Figure 9D** shows that the faint component has a larger k/h ratio (1.40) than the bright prominence (mainly between 1.2 and 1.3), which suggests that the faint component has a lower opacity. It should be noticed that the k/h ratios vary for different prominences with different viewing angles Reference [11]. reported the k/h value around 1.4 in the main body of an eruptive prominence in quiet region, but in the erupting prominence studied by Reference [10]; the intensity ratio of the primary bright component varies from 1.4 to 1.9.

Prominence Mg II k radiation is partly from the emission of local plasma, and partly from the scattering of the chromospheric radiation [7, 34]. In our observations, the faint component can absorb or scatter the light from the bright part behind. Using non-LTE radiative transfer techniques Reference [20], simulated emergent Mg II k and h lines in solar disk; the authors found that Mg II k core intensity is weak if the line core forms at a high position due to a low density and three-dimensional scattering, although temperature increases along height in the chromosphere. In our observations, the low emission (**Figure 7E2-E4**) and deep central reversal (**Figure 7D3**) of the faint component possibly result from the scattering of low-density plasma. In addition, line width is mainly determined by plasma temperature and micro-turbulence. The narrow Mg II k line profiles suggest that the faint component is mainly prominence core, whose temperature is lower than the PCTR.

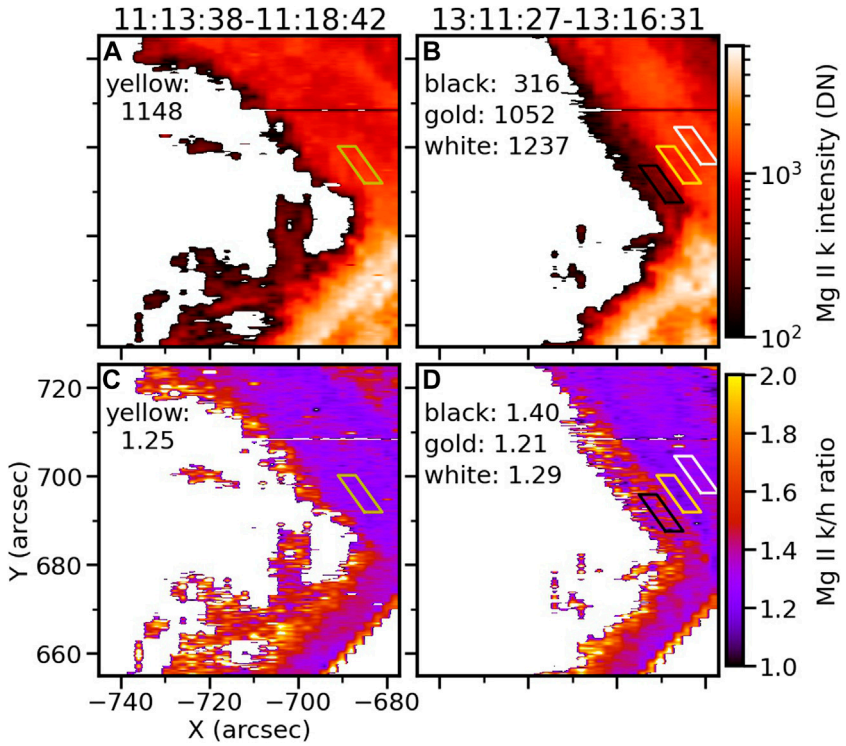

FIGURE 9 | Images of integrated uncalibrated intensity of the Mg II k line **(A–B)** and the Mg II k/h intensity ratio **(C–D)**. Mean values of the marked regions are noted in each panel.

TABLE 2 | Main observational results of this work.

Prominence eruption	(1) Slow-rise phase (2) Fast-rise phase
Evolution of spectra	(1) Opposite Doppler shifts with respect to the prominence axis in slow-rise phase (2) Dominantly red-shifted around the onset of fast-rise phase (3) Dominantly blue-shifted during prominence eruption
Faint component	Faint and narrow features in the Mg II k line Large red shifts (~ 60 km s^{-1}) around the onset of fast-rise phase Darkening and expansion in AIA 304 Å

Therefore, we propose that the faint component consists of low-density and cold plasma, which appear due to the expansion of the prominence core during the prominence eruption. In this process, the flows move fast along the prominence spine and result in significant Doppler shifts. However, non-LTE modeling is necessary to give a strict explanation on the characteristics of the AIA 304 Å and IRIS Mg II k observations.

5 CONCLUSION

We studied spectral evolution of an eruptive polar crown prominence using its IRIS observations in the Mg ii and Si iv lines and AIA EUV images. The main observational results of this work are listed in **Table 2**. The AIA observations suggest that the prominence experiences a slow- and fast-rise phase before **it** leaves the FOV of AIA. Simultaneously, the variation of Doppler shifts of the erupting prominence could be divided into three periods. In the first period, more than 2 h before the onset of the fast-rise phase, opposite Doppler shifts at the two sides of the prominence axis are found with maximum LOS velocity between 20–30 km s^{-1}. In the second period, around the onset of the fast-rise phase, the whole prominence gets to be red-shifted gradually. In the third period, the prominence is dominantly blue-shifted. The possible cause of the opposite Doppler shifts in the first period is large-scale counter-streaming, or unidirectional flows along the prominence spine (as a flux rope). More observations are necessary to determine which mechanism results in the opposite shifts, then reveal the mode of flows within the prominence spine. Besides, the opposite Doppler shifts of the

faint component during the fast-rise phase may result from the untwisting motion of the erupting prominence. The obvious red shifts in the second period may reveal mass drainage along the prominence spine due to the elevation of the prominence, and the mass drainage might accelerate the prominence eruption in return. The blue shifts in the last period is likely to result from the eruption of the prominence toward the observer.

During the second period, a faint component appears in AIA 304 Å, SJI 2796 and 1400 Å. The faint component has a narrow line profile, is initially red-shifted with a typical LOS velocity of 60 km s^{-1}. The Mg II k/h ratio of the faint component (~ 1.40) is larger than that of the bright component (between 1.2 and 1.3), which suggests that the faint component has a lower opacity. We also observed the darkening and expansion of the faint component in AIA 304 Å images. On the basis of these characteristics, we propose that the faint component is composed of low-density and cold plasma due to the expansion of the prominence during eruption.

Hence we can relate the evolution of the spectra and the formation of the faint component to the prominence eruption. The opposite Doppler shifts are properties of the polar crown prominence that we studied. When the prominence approaches eruption, the prominence spine elevates and expands, and the acceleration of the mass drainage causes the obvious red shifts. Simultaneously, a faint region along the prominence spine forms and gets darker due to the decreasing of the plasma density during the spine expansion. Finally, the acceleration of the prominence eruption results in the blue shifts. Despite the consistence of above explanations, however, non-LTE radiative transfer simulations in future are necessary to interpret the observational characteristics of the Mg II k line and AIA 304 Å images.

DATA AVAILABILITY STATEMENT

Publicly available datasets were analyzed in this study. This data can be found here: https://iris.lmsal.com/search.

AUTHOR CONTRIBUTIONS

JX processed the observational data, decided the main content of the paper, plotted figures, and wrote the article. HL selected the topic, joined discussion, and modified the article. YS joined discussion, offered ideas about the explanation on the observed phenomena, and modified the article.

FUNDING

This work is supported by the NSFC grants (11427803, U1731241, U1631242, 11820101002) and by CAS Strategic Pioneer Program on Space Science, grant Nos. XDA15052200, XDA15320103, XDA15320300, and XDA15320301.

ACKNOWLEDGMENTS

The authors thank the reviewers for their suggestions, some findings and ideas in this paper are proposed by them. JX thanks Jean-Claude Vial, Yingna Su, and Ping Zhang for discussion, thanks Ying Li and Hui Tian for a guidance on processing IRIS data. We thank the IRIS, AIA, and HMI teams for providing the data. YS acknowledges the Jiangsu Double Innovation Plan.

REFERENCES

1. Labrosse N, Heinzel P, Vial JC, Kucera T, Parenti S, Gunár S, et al. Physics of Solar Prominences: I—Spectral Diagnostics and Non-LTE Modelling. *Space Sci Rev* (2010) 151:243–332. doi:10.1007/s11214-010-9630-6
2. Parenti S. Solar Prominences: Observations. *Living Rev Solar Phys* (2014) 11:1. doi:10.12942/lrsp-2014-1
3. Vial J-C, and Engvold O. *Solar Prominences* (2015) 415.
4. Chen P-F, Xu A-A, and Ding M-D. Some Interesting Topics Provoked by the Solar Filament Research in the Past Decade. *Res Astron Astrophys* (2020) 20: 166. doi:10.1088/1674-4527/20/10/166
5. De Pontieu B, Title AM, Lemen JR, Kushner GD, Akin DJ, Allard B, et al. The Interface Region Imaging Spectrograph (IRIS). *Sol Phys* (2014) 289:2733–79. doi:10.1007/s11207-014-0485-y
6. Schmieder B, Tian H, Kucera T, López Ariste A, Mein N, Mein P, et al. Open Questions on Prominences from Coordinated Observations by IRIS, Hinode, SDO/AIA, THEMIS, and the Meudon/MSDP. *A&A* (2014) 569:A85. doi:10.1051/0004-6361/201423922
7. Vial J-C, Pelouze G, Heinzel P, Kleint L, and Anzer U. Observed IRIS Profiles of the H and K Doublet of Mg Ii and Comparison with Profiles from Quiescent Prominence NLTE Models. *Sol Phys* (2016) 291:67–87. doi:10.1007/s11207-015-0820-y
8. Okamoto TJ, Liu W, and Tsuneta S. Helical Motions of Fine-structure Prominence Threads Observed by Hinode and IRIS. *ApJ* (2016) 831:126. doi:10.3847/0004–637X/831/2/126
9. Ruan G, Schmieder B, Mein P, Mein N, Labrosse N, Gunár S, et al. On the Dynamic Nature of a Quiescent Prominence Observed by IRIS and MSDP Spectrographs. *ApJ* (2018) 865:123. doi:10.3847/1538-4357/aada08
10. Liu W, De Pontieu B, Vial J-C, Title AM, Carlsson M, Uitenbroek H, et al. First High-Resolution Spectroscopic Observations of an Erupting Prominence within a Coronal Mass Ejection by the Interface Region Imaging Spectrograph (IRIS). *ApJ* (2015) 803:85. doi:10.1088/0004-637X/803/2/85
11. Zhang P, Buchlin É, and Vial JC. Launch of a CME-Associated Eruptive Prominence as Observed with IRIS and Ancillary Instruments. *A&A* (2019) 624:A72. doi:10.1051/0004-6361/201834259
12. Lörinčík J, Dudík J, Aulanier G, Schmieder B, and Golub L. Imaging Evidence for Solar Wind Outflows Originating from a Coronal Mass Ejection Footpoint. *ApJ* (2021) 906:62. doi:10.3847/1538-4357/abc8f6
13. Lemen JR, Title AM, Akin DJ, Boerner PF, Chou C, Drake JF, et al. The Atmospheric Imaging Assembly (AIA) on the Solar Dynamics Observatory (SDO). *Sol. Phys.* (2012) 275:17–40. doi:10.1007/s11207-011-9776-8
14. Pesnell WD, Thompson BJ, and Chamberlin PC. The Solar Dynamics Observatory (SDO). *Sol Phys* (2012) 275:3–15. doi:10.1007/s11207-011-9841-3
15. Scherrer PH, Schou J, Bush RI, Kosovichev AG, Bogart RS, Hoeksema JT, et al. The Helioseismic and Magnetic Imager (HMI) Investigation for the Solar Dynamics Observatory (SDO). *Sol Phys* (2012) 275:207–27. doi:10.1007/s11207-011-9834-2
16. Schwartz P, Heinzel P, Schmieder B, and Anzer U. Study of an Extended EUV Filament Using SoHO/SUMER Observations of the Hydrogen Lyman Lines. *A&A* (2006) 459:651–61. doi:10.1051/0004-6361:20065619

17. Schwartz P, Gunár S, and Curdt W. Non-LTE Modelling of Prominence fine Structures Using Hydrogen Lyman-line Profiles. *A&A* (2015) 577:A92. doi:10.1051/0004-6361/201425138
18. Gunár S, Heinzel P, Anzer U, and Schmieder B. On Lyman-line Asymmetries in Quiescent Prominences. *A&A* (2008) 490:307–13. doi:10.1051/0004-6361:200810127
19. Gunár S, Schwartz P, Schmieder B, Heinzel P, and Anzer U. Statistical Comparison of the Observed and Synthetic Hydrogen Lyman Line Profiles in Solar Prominences. *A&A* (2010) 514:A43. doi:10.1051/0004-6361/200913411
20. Leenaarts J, Pereira TMD, Carlsson M, Uitenbroek H, and De Pontieu B. The Formation of IRIS Diagnostics. II. The Formation of the Mg II H&k Lines in the Solar Atmosphere. *ApJ* (2013) 772:90. doi:10.1088/0004-637X/772/2/90
21. Uitenbroek H. The Accuracy of the Center-of-Gravity Method for Measuring Velocity and Magnetic Field Strength in the Solar Photosphere. *ApJ* (2003) 592:1225–33. doi:10.1086/375736
22. Cheng X, Zhang J, Ding MD, Olmedo O, Sun XD, and Guo Y. Investigating Two Successive Flux Rope Eruptions in a Solar Active Region. *ApJ* (2013) 769:L25. doi:10.1088/2041-8205/769/2/L25
23. Su Y, van Ballegooijen A, McCauley P, Ji H, Reeves KK, and DeLuca EE. Magnetic Structure and Dynamics of the Erupting Solar Polar Crown Prominence on 2012 March 12. *ApJ* (2015) 807:144. doi:10.1088/0004-637X/807/2/144
24. Chen PF, Harra LK, and Fang C. Imaging and Spectroscopic Observations of a Filament Channel and the Implications for the Nature of Counter-streamings. *ApJ* (2014) 784:50. doi:10.1088/0004-637X/784/1/50
25. Ouyang Y, Zhou YH, Chen PF, and Fang C. Chirality and Magnetic Configurations of Solar Filaments. *ApJ* (2017) 835:94. doi:10.3847/1538-4357/835/1/94
26. Zirker JB, Engvold O, and Martin SF. Counter-streaming Gas Flows in Solar Prominences as Evidence for Vertical Magnetic fields. *Nature* (1998) 396:440–1. doi:10.1038/24798
27. Lin Y, Engvold OR, and Wiik JE. Counterstreaming in a Large Polar Crown Filament. *Sol Phys* (2003) 216:109–20. doi:10.1023/A:1026150809598
28. Ahn K, Chae J, Cao W, and Goode PR. Patterns of Flows in an Intermediate Prominence Observed Byhinode. *ApJ* (2010) 721:74–9. doi:10.1088/0004-637X/721/1/74
29. Shen Y, Liu Y, Liu YD, Chen PF, Su J, Xu Z, et al. Fine Magnetic Structure and Origin of Counter-streaming Mass Flows in a Quiescent Solar Prominence. *ApJ* (2015) 814:L17. doi:10.1088/2041-8205/814/1/L17
30. Li LP, Peter H, Chen F, and Zhang J. Conversion from Mutual Helicity to Self-Helicity Observed with IRIS. *A&A* (2014) 570:A93. doi:10.1051/0004-6361/201424377
31. Li LP, and Peter H. Plasma Injection into a Solar Coronal Loop. *A&A* (2019) 626:A98. doi:10.1051/0004-6361/201935165
32. Zou P, Fang C, Chen PF, Yang K, and Cao W. Magnetic Separatrix as the Source Region of the Plasma Supply for an Active-Region Filament. *ApJ* (2017) 836:122. doi:10.3847/1538-4357/836/1/122
33. Fan Y. Simulations of Prominence Eruption Preceded by Large-Amplitude Longitudinal Oscillations and Draining. *ApJ* (2020) 898:34. doi:10.3847/1538-4357/ab9d7f
34. Heinzel P, Vial JC, and Anzer U. On the Formation of Mg Ii H and K Lines in Solar Prominences. *A&A* (2014) 564:A132. doi:10.1051/0004-6361/201322886

Conflict of Interest: The authors declare that the research was conducted in the absence of any commercial or financial relationships that could be construed as a potential conflict of interest.

Publisher's Note: All claims expressed in this article are solely those of the authors and do not necessarily represent those of their affiliated organizations, or those of the publisher, the editors and the reviewers. Any product that may be evaluated in this article, or claim that may be made by its manufacturer, is not guaranteed or endorsed by the publisher.